

Supporting Information for
Realization of Zero-Refractive-Index Lens with Ultralow Spherical
Aberration

Xin-Tao He ^{1,3}, Zhi-Zhen Huang ^{1,2,4}, Ming-Li Chang ^{1,3}, Shao-Zeng Xu ^{1,2}, Fu-Li Zhao^{1,3},
Shao-Zhi Deng ^{1,2,4}, Jun-Cong She ^{1,2,4,5,†}, and Jian-Wen Dong ^{1,3,*}

1. State Key Laboratory of Optoelectronic Materials and Technologies, Sun Yat-sen University, Guangzhou 510275, China
 2. Guangdong Province Key Laboratory of Display Material and Technology, Sun Yat-sen University, Guangzhou 510275, China
 3. School of Physics, Sun Yat-sen University, Guangzhou 510275, China
 4. School of Electronics and Information Technology, Sun Yat-sen University, Guangzhou 510275, China
 5. Sun Yat-sen University-Carnegie Mellon University (SYSU-CMU) Shunde International Joint Research Institute, Shunde 528300, China
- † Email: shejc@mail.sysu.edu.cn
* Email: dongjwen@mail.sysu.edu.cn

Keywords: zero index, low aberration, silicon photonics, metamaterial

Appendix A: Effective Refractive Index and Longitudinal Spherical Aberration of Plane-Concave Lens

Consider a plane-concave lens filling with low-index medium ($n_{eff} < 1$) in air background. Figure S1a describes the propagation behaviors of light with ray tracing method. The curvature radius of the concave lens is R , and point O is the curvature center. Assume an off-axial beam (purple ray) with off-axial distance H illuminating to the optical lens, the exit beam will be convergent at the focal point S . According to geometric optics, the distance from the focal point S to the curvature center O can be described by the following expression,

$$\Delta_S = \frac{H}{\tan(\alpha - \beta)} - \sqrt{R^2 - H^2}, \quad (S1)$$

where α and β are the angles of incident and exit ray, respectively. With a substitution of Snell's law, i.e. $n_{eff} \sin \alpha = n_{eff} H / R = \sin \beta$, the expression of eq S1 can be rewritten as,

$$\Delta_S = R \frac{n_{eff}}{1 - n_{eff}} \frac{\sqrt{1 - (n_{eff} H / R)^2} + n_{eff} \sqrt{1 - (H / R)^2}}{1 + n_{eff}}. \quad (S2)$$

We can see that the position of focal spot is determined by the effective refractive index of the plane-concave lens and the off-axial distance. Particularly, with consideration of paraxial approximation, i.e. $H \sim 0$, the expression for paraxial light can be simplified to

$$\Delta_S \approx \Delta_L = R \frac{n_{eff}}{1 - n_{eff}}. \quad (S3)$$

Note that eq S3 represents the deformation of Lens' maker formula, which is only valid for paraxial illumination (yellow ray in Figure S1a). Note also that the difference between Δ_S and Δ_L will give rise to longitudinal spherical aberration (LSA), yielding

$$LSA = 10 \lg \left| \frac{\Delta_s - \Delta_L}{R} \right| = 10 \lg \left| \frac{n_{eff}}{1 - n_{eff}} \left(\frac{\sqrt{1 - (n_{eff} H / R)^2} + n_{eff} \sqrt{1 - (H / R)^2}}{1 + n_{eff}} - 1 \right) \right|, \quad (S4)$$

which is normalized by the curvature radius R and in dB scale. Figure S1b shows the quantitative LSA of the plane-concave lens as a function of refractive index and off-axial distance. The value of LSA increases with the off-axial distance H , except for near-zero refractive index. In other words, LSA is possible to vanish when constructing the plane-concave lens by near-zero-index medium.

Alternatively, with a combination of Snell's law and eq S1, we can simply deduce the effective refractive index (ERI) of the metalens as the following expression,

$$n_{eff} = \frac{R}{H} \sin \left[\arcsin \left(\frac{H}{R} \right) - \arctan \left(\frac{H}{\sqrt{R^2 - H^2} + \Delta_s} \right) \right]. \quad (S5)$$

which is the same as eq 2 in the text. With a view to optical characterization, we finally select off-axial illuminations for the measurement of focal point so as to obtain the refractive index.

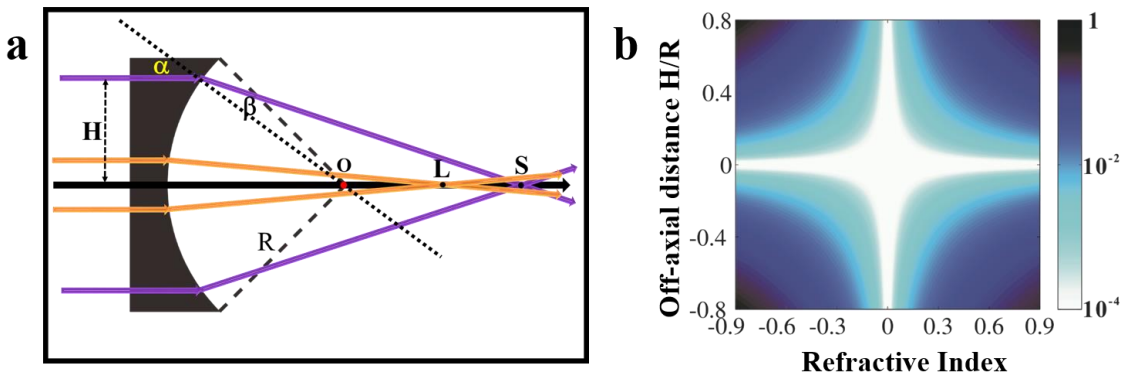


Figure S1. Longitudinal spherical aberration in optical plane-concave lens. (a) Geometric optics diagram of light focusing effect. Point L represents the focal spot illuminated by paraxial light (yellow rays), while point S is the focal spot of off-axial light (purple rays). Note that such two points do not overlap, leading to longitudinal spherical aberration (LSA). (b) Quantitative LSA of the plane-concave lens as a function of refractive index and off-axial distance. The value of LSA increases with off-axial distance, except for

near-zero-index medium.

Appendix B: Numerical simulation

In this work, all of band calculations were implemented by MIT Photonic-Bands (MPB)¹ and all of FDTD calculations were implemented by MIT electromagnetic equation propagation (MEEP)². For the 3D transmittance spectra in Figures 2f and S2, there are 10 rods along x direction with the same bulk parameters to the zero-index lens. Bloch boundary conditions are imposed on the surfaces perpendicular to x-z plane, while other four surfaces are set by perfectly matched layer (PML) absorbing boundary. It means that we are dealing with a semi-infinite structure along y direction. The incident plane wave is set as the same height to silicon rods, and the other side is a monitor plane to detect the energy passing through the device.

Appendix C: Effective Index of Cone-Shaped Nanopillars

In our design, we consider the nanopillars with uniform profiles along the axial (z) direction, as shown in Figure 2 of main text. However, the profile of each nanopillar (the inset of Figure S2g) has the type of cone, rather than cylinder. The diameter of each pillar is typically 310 nm at the top while 400 nm at the base, deviated from the ideal radius of 335 nm. The purpose of this section is to study the optical properties of zero-index photonic crystal, e.g. effective refractive index measurement, after considering the nanopillars with cone shape.

Photonic Dirac cone at the center of Brillouin zone emerges as a consequence of accidental degeneracy at a particular diameter of the nanopillar³. Here, the band structure of zero-index photonic crystal in Figure S2b shows a triply-degenerate point at Γ point at

the wavelength of 1490 nm. The lattice constant, the diameter and relative permittivity of silicon are set at $a = 818$ nm, $d = 335$ nm and $\epsilon = 11.7$, respectively. Two linear dispersions (red solid lines) intersect at the triply-degenerate point with a third flat band (green dash line). However, such triply-degenerate point will break up when the diameter of the nanopillar deviates from 335 nm. When the diameter increases to $d = 400$ nm (Figure S2c), the triply-degenerate point is decoupled into a doubly-degenerate point (two dipolar modes) and a single mode (monopolar mode), exhibiting a complete gap. Similar results can also be observed in Figure S2a for the case of $d = 310$ nm, but there is lack of complete gap (only directional gap) due to the flat band.

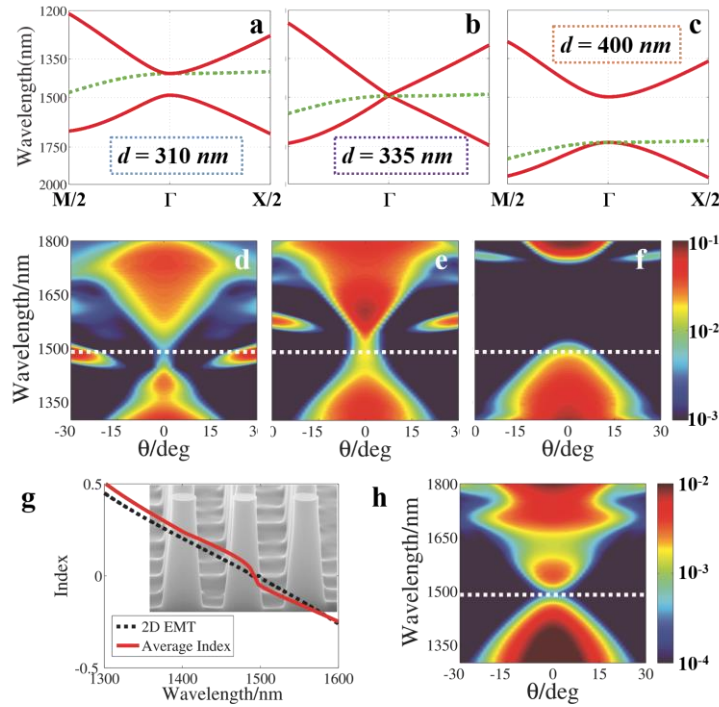


Figure S2. Optical properties of all-silicon photonic crystals both in 2D infinitely-thick models and 3D wavelength-order-thick systems. (a-c) 2D bulk bands of square lattice photonic crystal with different diameters d . Photonic Dirac cone can be observed in (b) due to accidental degeneracy, but broken up in (a) and (c) when the diameter of the nanopillar deviates from 335 nm. (d-f) Quasi-3D transmittance of the wavelength-order-thick ($1.7 \mu\text{m}$) nanopillar array as a function of incident angle and wavelength, where the diameters of cylindrical pillars are correspondence with (a-c) respectively. (g) The effective refractive index retrieved by effective medium theory based on Mie resonance. Black dash corresponds to 2D model with cylindrical pillars, while the red solid is the

average refractive index of cone-shaped pillar array with a combination of multilayer approximation. (h) Re-simulation of 3D transmittance in cone-shaped nanopillar array. The conical-like transmission spectra can be observed near the Dirac wavelength of 1490 nm, although the total energy has one order of magnitude less than the ideal case (e)

Figures S2d-f present quasi-3D transmittance of ten-period silicon pillars as a function of incident angle and wavelength, where the diameters of cylindrical pillars are correspondence with Figures S2a-c, respectively. The thickness of nanopillars in these 3D calculations are set on the order of wavelength (1.7 μm). See Appendix B for numerical setup. The transmission spectra illustrate the optical responses in this finitely-thick system are similar to bulk bands of the 2D photonic crystals. In this way, the deviations of quasi-3D systems have been recovered when the nanopillars are high on the order of wavelength. Due to the imperfect fabrication, we also take cone-shaped structure into the re-simulation of 3D transmittance, as shown in Figure S2h. The nanopillars have the same thickness to cylindrical shape, but perform non-uniform profile along the axial (z) direction (310 nm at the top while 400 nm at the base). The conical-like transmission spectra can be observed near the Dirac wavelength of 1490 nm, although the total energy has one order of magnitude less than the ideal case (Figure S2e).

Finally, we will discuss how such cone-shaped pillars have an influence on the effective refractive index. Cylindrical pillar PCs can be described by effective medium theory (EMT) based on Mie resonance⁴. Consider square lattice photonic crystals of silicon cylindrical pillars in air background, the effective indices are related to diameter d and wavelength λ , i.e. $\varepsilon_{\text{eff}}(d, \lambda), \mu_{\text{eff}}(d, \lambda)$. The effective refractive index is then retrieved as follow,

$$n_{\text{eff}}(d, \lambda) = \sqrt{\varepsilon_{\text{eff}}(d, \lambda) \mu_{\text{eff}}(d, \lambda)}. \quad (\text{S6})$$

Black dash curve in Figure S2g presents the ideal case of $d = 335$ nm, indicating zero index emerges near the Dirac wavelength of 1490 nm. In practice, EMT is not straightforward for the pillars with cone shape. But each coned pillar can be discrete into a set of short-enough cylinder pillars with gradient diameters from d_{\min} (310nm) to d_{\max} (400nm). Then, the average refractive index of the coned pillar array can approximate to

$$\bar{n}_{eff}(\lambda) = \frac{1}{N_d} \sum_{d=310nm}^{400nm} \text{Re}[n_{eff}(d, \lambda)], \quad (S7)$$

where N_d is the number of short-enough cylinder pillars. The calculated result is shown in the red curve of Figure S2g, and $N_d = 91$ is large enough to guarantee the convergence of summation in eq S7. The near-zero refractive index can also be seen near the Dirac wavelength, although most of the values are deviated from the ideal case (black dash). Compared with the 3D transmittance of Figure S2h, we can conclude that the near-zero-index feature still exists in such cone-shaped structure both below and near the Dirac wavelength. In the long wavelength region (upon 1600 nm), the system cannot be mapped to EMT with two reasons. One is the excitation of quasi-flat band, and the other is the interference between the passing band (e.g. Figure S2f) and the stop band (e.g. Figure S2d).

Appendix D: Homogenization of photonic crystal with wavelength-order-periodicity

Generally speaking, effective medium theory is valid for periodic structure under the condition of long-wavelength limit $k_0 a \ll 1$, where k_0 is the wave number in background medium and a is the lattice constant⁵. Later, effective medium theory was extended to the structure with wavelength-order-periodicity under monopolar and dipolar responses⁴,

when the limit was modified to $k_{eff}a \ll 1$. Here, k_{eff} is the effective wavenumber inside the periodic structure. In other words, a periodic structure operating at near zero k_{eff} can be homogenized as an effective medium, beyond the long-wavelength limit.

In this work, we focus on the Dirac cone at the Brillouin zone center that $k_{eff} \sim 0$ and the triply mode is due to accidentally degenerate from the monopolar and dipolar modes. So such photonic crystal near Γ point can be effectively viewed as a type of metamaterials, even it has a half-wavelength-order lattice constant. To verify the homogenization, Figure S3a shows E_z profiles inside the zero-index photonic crystal, which is constructed by array of silicon rods with the same geometrical parameters as those in fabrication. It is obvious to see from down panel in Figure S3a, that each unit cell maintains in-phase resonance with one another, resulting in near-zero phase change. As a consequence, the propagating wave has the same phase as the incident port, when it exits from the right boundary of the photonic crystal and air. This is similar to the case of the ideal zero-index medium (Figure S3b), indicating that such photonic crystal with wavelength-order-periodicity can be considered as an effective near-zero bulk medium. Note that the energy within zero-index photonic crystal decays along propagating direction due to out-of-plane radiative loss. More details about the analysis of radiative loss can be seen in Appendix E.

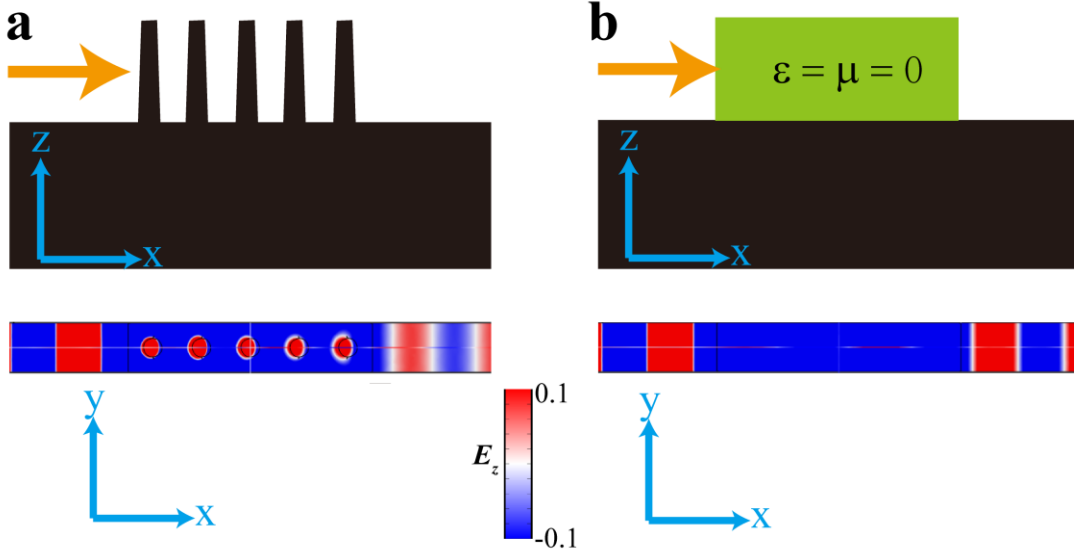


Figure S3. E_z field profiles in the zero-index photonic crystal with wavelength-order-periodicity and the conceptual zero-index metamaterial. (a) Front view of 3D structure and top view of the corresponding field profile. The 3D structure is a nanopillars array with $1.7\mu\text{m}$ height, 5 rows in x axis, and infinite periodicity along y axis. The incident plane waves propagate along +x direction with the Dirac wavelength of 1490 nm. 3D finite element simulation shows that each unit cell maintains in-phase resonance with one another and thus leads to near-zero phase change, although the energy decays along propagating direction due to out-of-plane radiative loss. (b) Same as (a) except that the photonic crystal is replaced by the ideal zero-index medium.

Appendix E: Analysis of propagation loss

As the photonic Dirac cone locates inside the light cone, the bulk states of the photonic crystal slab with finite thickness should have strong radiation towards out-of-plane space, leading to propagation loss. In this section, we will analyze the decay characteristics of the radiative zero-index modes using 3D FDTD simulation. Figure S4a shows the numerical setup in x-y plane. The periodic boundary conditions are imposed on the surfaces perpendicular to x-z plane, while other four surfaces are set by perfectly matched layer (PML) absorbing boundary. It means that we are dealing with a semi-infinite structure along y direction. The silicon rods are set as the same parameters as the fabricated nanopillars and labeled as $i_r = 1, 2, 3 \dots 60$. An incident plane wave with the

same height to silicon rods is from the left and passes through the zero-index photonic crystal.

Figures S4b and S4c present electromagnetic energy patterns w in two different regions, showing the obvious difference between the short-range (Figure S4b) and the long-range region (Figure S4c). To quantitatively analyze the out-of-plane radiation, we plot the average energy $\bar{w} = \frac{1}{V} \iiint_{rod} w dV$ as a function of propagation length L , depicted in Figure S4d, where V is the 3D volume of the rod. Interestingly, there are two regimes of decay behaviors. At the short-range region of $L \leq 11a$, \bar{w} manifests the form of log-linear decay with about 3.49dB/a propagation loss. However, it turns to a quasi-power-law decay with a function of $1/(L/a)^4$, when $L > 11a$. The average propagation loss is about 0.6dB/a. Such two-segment decay behavior seems to be typical for the radiative mode in open 2D system, as similar issue has been found in 2D metal nanoparticle quasicrystalline arrays⁶. We believe that this loss may be further minimum by increasing the thickness of nanopillars or by fabricating the device on SOI platform.

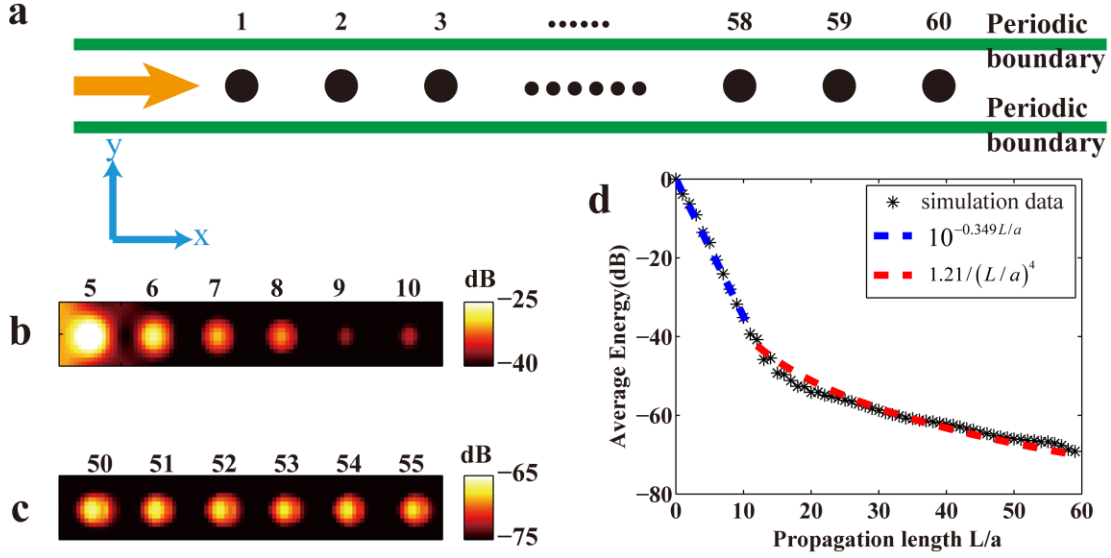


Figure S4. Analysis of out-of-plane radiation loss. (a) Schematic of numerical setup in x-y plane. There are 60 rows of nanopillars along the propagating direction, labeled as $i_r = 1, 2, 3 \dots 60$. (b-c) Electromagnetic energy patterns w in two different regions. (d) Average energy \bar{w} in dB scale as a function of the propagation length. The average energy has two-segment decay behaviors with a critical transition point of $L \sim 11a$, which is similar to the case of plasmonics nanoparticle array in Ref. S6.

Appendix F: Experimental Setup for Optical Characterization

We setup a microscope system to characterize light propagation through device, as depicted in Figure S5. In order to retrieve steady states, a tunable laser (Santec TSL-510) was used to generate continuous waves. The incident light was firstly launched into a polarizer to select TM-polarization mode, and then couple to the device with the aid of aspheric lens. Some of in-plane waves turn to be out-of-plane radiation after passing through device and hitting the irregular substrate. Consequently, the scattered light could be collected by a 50X microscope objective and imaged by using a charge-coupled device (CCD) camera (Electrophysics MicronViewer 7290A).

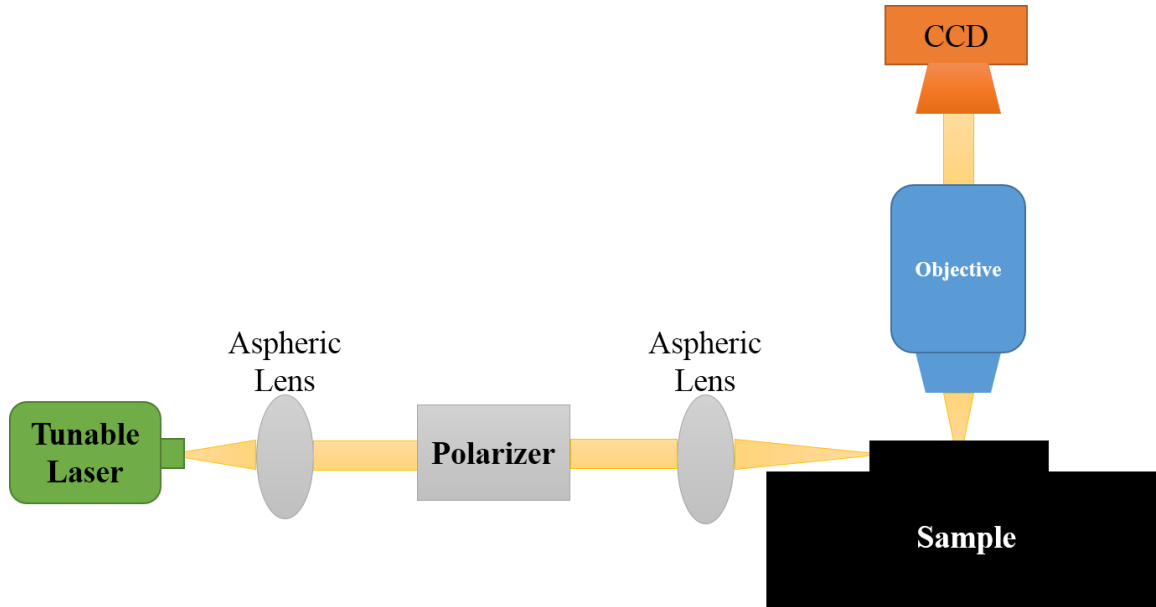


Figure S5. Schematic diagram of experimental setup for optical microscope images. A near IR continuous wave was firstly launched into a polarizer to select TM-polarization mode, and then couple to the device with the aid of aspheric lens. After passing through device and hitting the irregular substrate, the scattered light turn to be out-of-plane radiation and could be collected by a 50X microscope objective and imaged by using a charge-coupled device (CCD) camera.

Appendix G: Incoherent Focusing Images

The optical microscope images of light propagation through the fabricated lens were observed by the setup in Figure S5. The results are illustrated in Figures S6a-S6c with the incident light wavelength of 1360nm (below Dirac wavelength). White solid lines indicate the location of the fabricated lens and the golden arrows are depicted the incident light. The light trajectory comes from the scattered signal passing through the device and reflecting by the irregular silicon substrate. With fine tuning the incident spot of light, the scattered light changes the direction and is convergent to the middle. After mixing the off-axial illumination patterns (e.g. Figures S6a and S6c) into a doubly composite image, the focal point is obviously observed. Note that the focal point is close to the curvature center of the output interface (the cross-point of the two dash lines in Figure S6d),

indicating that the effective index of the fabricated lens is $n_{eff} < 1$. In comparison, the triply composite image, i.e., the mixture of Figures S6a, S6b, and S6c, is also depicted in Figure S6e, suffering from LSA so that the focusing point will be more difficult to be measured. Two-dimensional FDTD simulation result in Figure S6f is used to compare with the experimental result. Three incoherent beams of Gaussian waves propagate from left side and then transform to a focal spot after passing through the device.

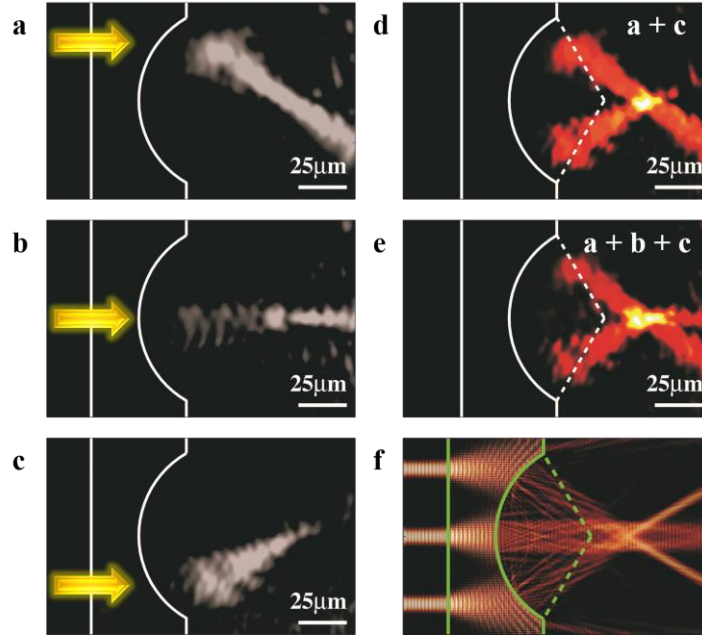


Figure S6. Optical microscope image of scattered light output from the fabricated zero-index lens at the wavelength of $\lambda = 1360$ nm. (a-c) Original microscope images for diverse incidence points. Golden arrows are superimposed on the structure to illustrate the incident light. White solid lines indicate the locations of sample. The light trajectory in these images results from the scattered light passing through the device and hitting the irregular substrate. (d) Composite image of off-axial illumination for (a) and (c). Two incoherent beams focus on a point near the center of concave surface. The focusing effect in our experiment indicates that the effective refractive index of this lens should be less than air. (e) Triply composite image for (a-c). Due to the interference of paraxial light and off-axial light, such focusing image suffers from LSA so that the position is more difficult to be measured. (f) Two-dimensional FDTD simulation result of the zero-index lens as the same parameters to (e).

Appendix H: Control Experiment

To experimentally compare with the anomalous focusing effect of zero-index concave

lens, we perform a control experiment on the same characterization setup with homogeneous silicon concave lens. Figure S7 shows the results at the operation wavelength of 1500 nm both in simulation (top row) and experimental measurement (down row). It is observed that three incoherent collimated beams turn to be divergent after passing through this high-index concave lens (Figures S7b and S7d). These results have a direct contrast with the convergent case of the zero-index concave lens (Figures S7a and S7c), confirming that the anomalous focusing effect in this work is related the near-zero index.

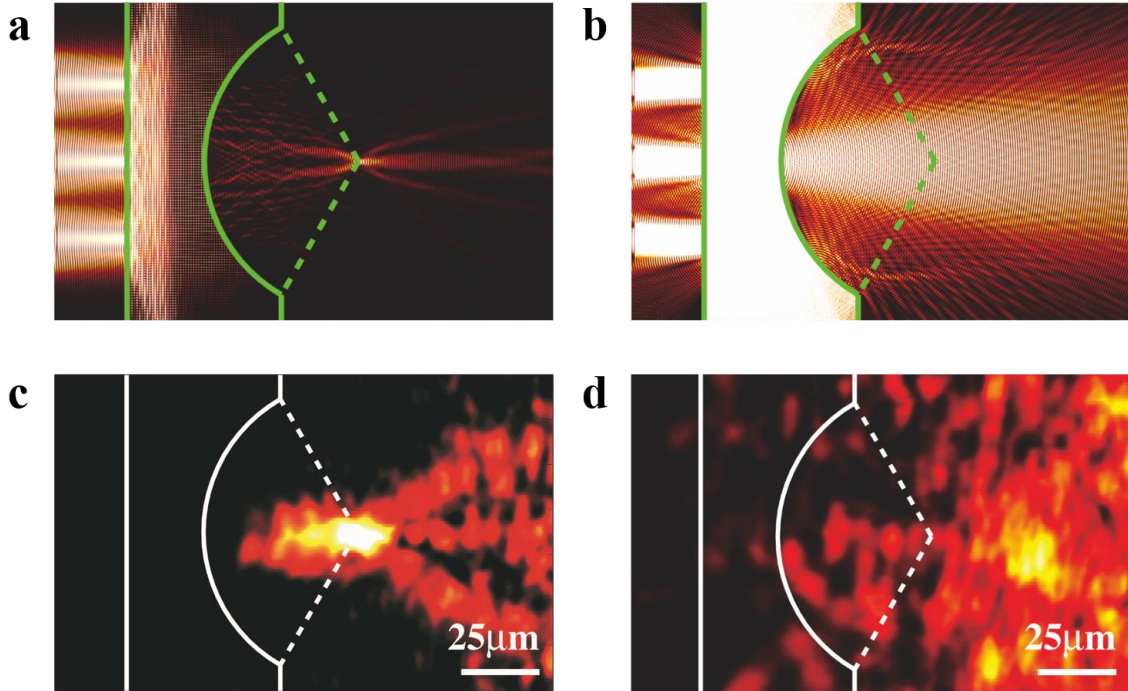


Figure S7. Total energy patterns of the control experiment between zero-index concave lens (left panel) and silicon concave lens (right panel) at the wavelength of $\lambda = 1500$ nm. (a-b) 2D FDTD simulation results excited by three incoherent beams of Gaussian sources. (c-d) Optical microscope images as the same experimental setup to Figure S6. As above demonstration, anomalous focusing effect can be observed in the zero-index lens (left panel). But the refracted beams turn to be divergent when replacing the device by silicon concave lens (right panel).

Appendix I: Evaluation Process of Measured Data

Here, we will perform how to quantitatively evaluate the focal points from the measured images, and to derive effective refractive index and longitudinal spherical aberration. At first, an integrating function $\bar{I}_s(x, N_y)$ is defined by averaging the spatial intensity $I_s(x, y)$ for doubly composite image (Figure S6d) within the region of $[-(N_y-1)/2, (N_y-1)/2]$, and thus the x location of the maximum value of $\bar{I}_s(x, N_y)$ is the focal point $\Delta_s(N_y)$. Then we have

$$\bar{I}_s(x, N_y) = \int_{-y_0}^{y_0} I_s(x, y) dy \approx \frac{1}{N_y} \sum_{y=-(N_y-1)/2}^{(N_y-1)/2} I_s(x, y). \quad (\text{S8})$$

Here, the optical axis is set as $y = 0$. Figures S8a-c plot the integrating function for $N_y = 11, 21, 31$, respectively. The focal point, i.e., the position of the peak, shifts a little for three different values of N_y , resulting in the errorbar of effective refractive index measurement in Figure 4a of the text.

In a similar way, we can retrieve the integrating function $\bar{I}_L(x, N_y)$ for triply composite image (Figure S6e), as illustrated in Figures S8d-f. Due to the interference of paraxial illumination, the positions of focal points $\Delta_L(N_y)$ will be deviated from the off-axial cases (Figures S8a-c) and suffer from longitudinal spherical aberration (LSA), yielding

$$LSA(N_y) = 10 \lg \left| \frac{\Delta_s(N_y) - \Delta_L(N_y)}{R} \right| \quad (\text{S9})$$

We should note that the LSA also shifts a little for three different values of N_y . This is the derivation of the errorbar of LSA measurement in Figure 4b of the text.

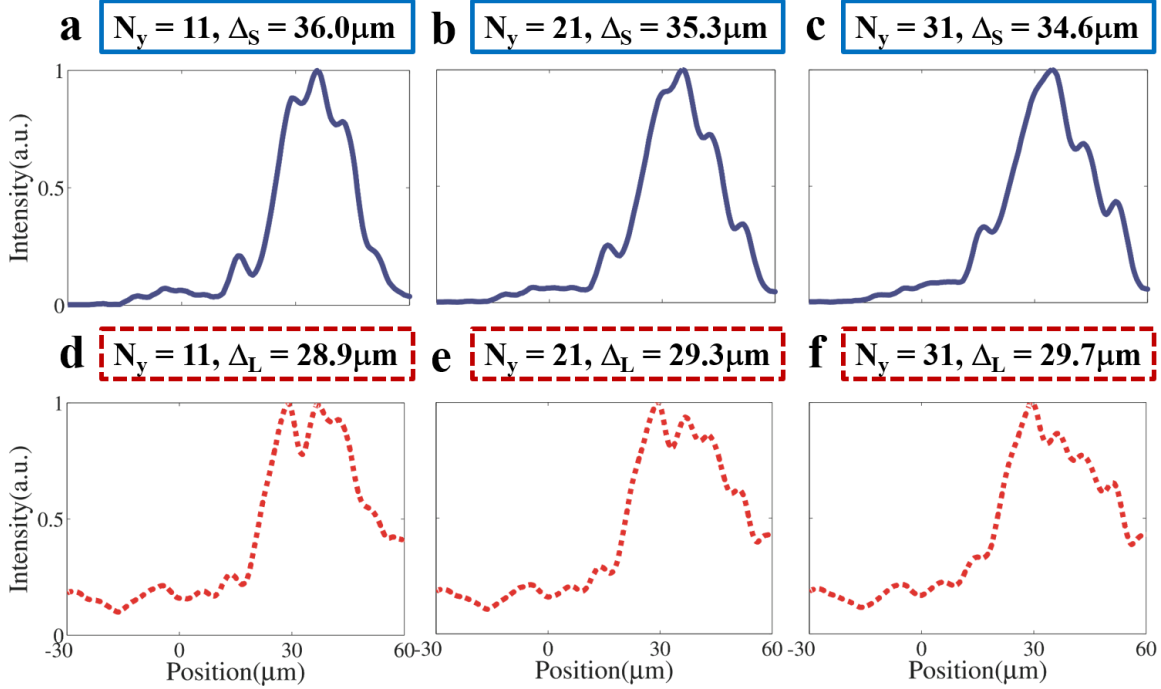


Figure S8. Intensity distribution of the focusing pattern along the optical axis at the wavelength of 1360 nm. (a-c) The intensity retrieved from off-axis illumination (Figure S6d) with a fixed y-integrating pixel. The intensity peaks indicate the position of focal points and the difference for each y-integrating pixel N_y shows the error bars of the refractive index measurement. (d-f) The intensity retrieved from triple composite image (Figure S6e) with different y-integrating pixel. Due to the interference of paraxial illumination, the positions of focal points will be deviated from the off-axis cases and suffer from longitudinal spherical aberration. Here, N_y is the number of y-integrating pixel, and Δ_S (Δ_L) is the distance from off-axis (mixed) focal point to the center of concave surface.

References

- (1) Johnson, S. G.; Joannopoulos, J. D. Block-iterative frequency-domain methods for Maxwell's equations in a planewave basis. *Optics Express* **2001**, 8, 173–190.
- (2) Oskooi, A. F.; Roundy, D.; Ibanescu, M.; Bermel, P.; Joannopoulos, J. D.; Johnson, S. G. MEEP: A flexible free-software package for electromagnetic simulations by the FDTD method. *Computer Physics Communications* **2010**, 181, 687–702.
- (3) Huang, X.; Lai, Y.; Hang, Z. H.; Zheng, H.; Chan, C. T. Dirac cones induced by accidental degeneracy in photonic crystals and zero-refractive-index materials. *Nat. Mater.* **2011**, 10, 582–586.
- (4) Wu, Y.; Li, J.; Zhang, Z.-Q.; Chan, C. T. Effective medium theory for magnetodielectric composites: Beyond the long-wavelength limit. *Phys. Rev. B* **2006**, 74, 085111.
- (5) Sarychev, A. K.; McPhedran, R. C.; Shalaev, V. M. Electrodynamics of metal-dielectric composites and electromagnetic crystals. *Phys. Rev. B* **2000**, 62, 85.

- (6) Dong, J.-W.; Fung, K. H.; Chan, C. T.; Wang, H.-Z. Localization characteristics of two-dimensional quasicrystals consisting of metal nanoparticles. *Phys. Rev. B* **2009**, 80, 155118.